Title

Visualization of superparamagnetic dynamics in magnetic topological insulators

Journal

Science Advances, 1(10)

ISSN

2375-2548

Authors

Lachman, Ella O
Young, Andrea F
Richardella, Anthony
et al.

Publication Date

2015-11-06

DOI

10.1126/sciadv.1500740

Peer reviewed

MATERIALS SCIENCE

10.1126/sciadv.1500740

Visualization of superparamagnetic dynamics in magnetic topological insulators

Ella O. Lachman,[1]* Andrea F. Young,[1,2]* Anthony Richardella,[3] Jo Cuppens,[1] H. R. Naren,[1] Yonathan Anahory,[1] Alexander Y. Meltzer,[1] Abhinav Kandala,[3] Susan Kempinger,[3] Yuri Myasoedov,[1] Martin E. Huber,[4] Nitin Samarth,[3] Eli Zeldov[1]†

Quantized Hall conductance is a generic feature of two-dimensional electronic systems with broken time reversal symmetry. In the quantum anomalous Hall state recently discovered in magnetic topological insulators, time reversal symmetry is believed to be broken by long-range ferromagnetic order, with quantized resistance observed even at zero external magnetic field. We use scanning nanoSQUID (nano–superconducting quantum interference device) magnetic imaging to provide a direct visualization of the dynamics of the quantum phase transition between the two anomalous Hall plateaus in a Cr-doped $(Bi,Sb)_2Te_3$ thin film. Contrary to naive expectations based on macroscopic magnetometry, our measurements reveal a superparamagnetic state formed by weakly interacting magnetic domains with a characteristic size of a few tens of nanometers. The magnetic phase transition occurs through random reversals of these local moments, which drive the electronic Hall plateau transition. Surprisingly, we find that the electronic system can, in turn, drive the dynamics of the magnetic system, revealing a subtle interplay between the two coupled quantum phase transitions.

INTRODUCTION

The integer quantum Hall effect (QHE), first observed in clean two-dimensional electronic systems at high magnetic fields (*1*), is the paradigmatic example of a topological phase: different integer QH states are characterized by identical symmetries but different integer topological quantum numbers η, with the quantized Hall resistance given by $R_{xy} = h/(\eta e^2)$ (*2*). However, Hall quantization may also occur in the absence of an external field as long as time reversal symmetry (TRS) is broken (*3*). This quantum anomalous Hall (QAH) state was recently realized experimentally (*4*–*9*), following theoretical proposals based on combining strong spin-orbit coupling with long-range ferromagnetic (FM) order in magnetically doped topological insulators (TIs) (*10*–*18*). The QH plateau transition represents the canonical example of a topological phase transition, described by the divergence of the localization length and a universal critical scaling of transport coefficients (*19*). Recent theoretical calculations show that under certain assumptions, the QAH plateau transition can be mapped onto the same network model used to describe the integer QH plateau transition, leading to the same scaling laws (*20*).

Although the electronic topological transition in QH and QAH systems, taken in isolation, can be viewed as identical, the two experimental systems differ in several key aspects. The QH plateau transition is a purely electronic effect, in which delocalization occurs against a background of quenched electronic disorder. In contrast, the QAH plateau transition results from two coupled quantum phase transitions: the field-driven magnetic transition of the FM order and the electronic transition that is driven by TRS breaking of the FM transition. The dynamics of the FM reversal can endow the QAH electronic transition with features that do not have an analog in QHE systems. Exactly at the transition, both systems can be understood as a network of domain walls—magnetic domain walls for the QAH and domain walls of a different filling factor in the QHE—that host counterpropagating chiral edge states. Crucially, however, in contrast to the QH plateau transition, which describes the phase diagram of the system in thermodynamic equilibrium, the FM domain structure in the QAH is metastable, leading to hysteresis and relaxation dynamics that can directly affect the electronic system. Moreover, the energy scale of the electronic delocalization transition and its critical scaling may depend on the details of the microscopic FM structure and on the scaling of the magnetic phase transition. Finally, the electronic system, which commonly mediates FM interactions in dilute magnetic systems, can in turn modify the phase transition of the magnetic system. Most previous studies of QAH systems have used electronic transport measurements to probe the combined effect of magnetic and electronic evolutions, making it difficult to disentangle the individual roles of the two phase transitions. Thus, exploring the reciprocal coupling of the magnetic and electronic quantum phase transitions requires selective measurement tools that can address the two systems independently.

RESULTS

Here, we combine electronic transport with a scanning superconducting quantum interference device (SQUID) of 200-nm diameter that resides on the apex of a quartz tip [SQUID-on-Tip (SOT)] (*21*, *22*) to simultaneously probe the magnetic and electronic transitions at ^{3}He temperatures in a 7–quintuple layer (QL)–thick $Cr_{0.1}(Bi_{0.5}Sb_{0.5})_{1.9}Te_3$ film grown by molecular beam epitaxy (MBE) on an $SrTiO_3$ substrate (Fig. 1). The large dielectric constant of the substrate allows effective control of the chemical potential through back gating. The hysteretic R_{xy} transition occurs at a coercive field of H_c = 130 mT at 250 mK (Fig. 1A). At elevated fields, the longitudinal resistance (R_{xx}) shows a pronounced dip as a function of the back-gate voltage at $V_g \approx 6$ V

[1]Department of Condensed Matter Physics, Weizmann Institute of Science, Rehovot 76100, Israel. [2]Department of Physics, University of California, Santa Barbara, Santa Barbara, CA 93106–9530, USA. [3]Department of Physics, Pennsylvania State University, University Park, PA 16802, USA. [4]Department of Physics, University of Colorado Denver, Denver, CO 80217, USA.
*These authors contributed equally to this work.
†Corresponding author. E-mail: eli.zeldov@weizmann.ac.il

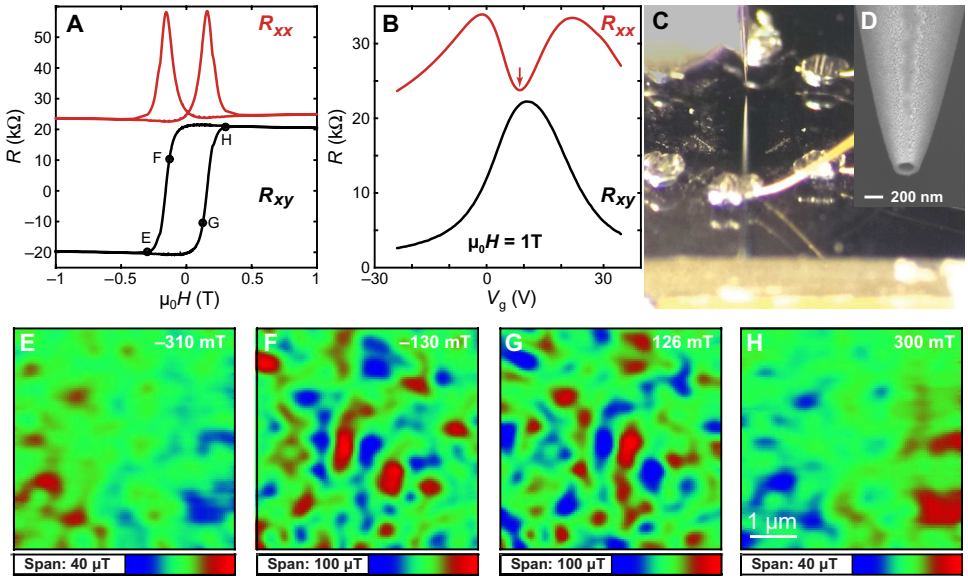

Fig. 1. Electrical transport and scanning magnetic imaging of 7-QL-thick $Cr_{0.1}(Bi_{0.5}Sb_{0.5})_{1.9}Te_3$ sample at T = 250 mK. (**A** and **B**) Transport measurements showing magnetic field dependence of R_{xx} (red) and R_{xy} (black) at V_g = 6 V (A) and the V_g dependence at 1 T (B). The dip in R_{xx} marked by the arrow shows the incipient QAH state. (**C**) Optical image of the sample and SOT showing the electrical contacts and the SOT reflection from the sample surface. (**D**) Electron micrograph of the SOT used for the magnetic imaging. (**E** to **H**) Scanning SOT images (5 × 5 μm^2) of the out-of-plane magnetic field $B_z(x,y)$ at ~300 nm above the sample surface at four antisymmetric locations along the magnetization loop marked in (A). Note strong anticorrelation between (E) and (H), and (F) and (G). Pixel size, 50 nm; pixel integration time, 10 ms.

due to an incipient QAH state (Fig. 1B). At the lowest measurement temperature (250 mK) used here, the sample we discuss does not yet show the fully developed QAH. This is similar to previous experiments on Cr-doped TI films (*4*–*9*) where quantized Hall resistance appears only at dilution refrigerator temperatures, far below the onset temperature of hysteretic magnetic behavior (*4*, *23*). Figure 1 (E to H) shows images of the local distribution of the magnetic field $B_z(x,y)$ in the sample at various points along the magnetization loop. We find $B_z(x,y)$ to be highly inhomogeneous at all fields, with peak contrast at H_c, where the average magnetization vanishes (Fig. 1, F and G). Submicrometer structure is evident even at fields corresponding to saturation of transport coefficients (Fig. 1, E and H), and images corresponding to opposite magnetization are highly anticorrelated on microscopic scales, including at full saturation. This suggests an inhomogeneous distribution of magnetic moments due to a random spatial distribution of the Cr dopants. Although high-resolution transmission electron microscopy measurements on our samples have yet to show any obvious evidence of Cr clustering (see fig. S1), we cannot preclude inhomogeneity at the nanoscale, akin to that found in other magnetically doped semiconductors such as Cr-doped ZnTe (*24*). Clear evidence of phase separation has only been seen in Cr-doped Bi_2Se_3 thin-film (*25*) samples that do not show the QAH state, whereas large nanoscale fluctuations in the local Cr density have been observed in Te-based samples (*26*) because of random doping that introduces strong disorder in the material (*27*).

In metallic FM thin films with out-of-plane magnetization, it is well established that magnetization reversal develops via the nucleation and propagation of domain walls separating regions of opposite magnetization. Such domain wall–mediated magnetization reversal has also been imaged in FM semiconductor films (*28*, *29*) at magnetic dopant concentrations comparable to those in our magnetic TI films. However, scanning SOT microscopy reveals a very different picture of the magnetization reversal process in magnetic TIs. Figure 2A shows a sequence of $B_z(x,y)$ images acquired for increasing values of $\mu_0 H$ near H_c. The five images appear almost identical; however, numerical subtraction of successive image data [$\Delta B_z(x,y)$, see Fig. 2B] reveals the underlying dynamic process. Instead of the anticipated domain wall motion, magnetization reversal occurs through a series of random events in which isolated nanoscale islands undergo a reversal of their out-of-plane magnetic moment (see movie S1). These islands are a system of small, weakly interacting magnetic moments (potentially FM single domains) that constitutes a superparamagnet. As we discuss below, our findings establish a direct microscopic observation of superparamagnetism in magnetically doped TI films. Our observations caution against drawing conclusions about the FM state solely from macroscopic magnetization probes (SQUID magnetometry, magneto-optical Kerr effect) that show square hysteresis loops with robust zero field remanence (*30*).

To quantify the superparamagnetic dynamics across the Hall plateau transition, we fit each of the local features in the $\Delta B_z(x,y)$ maps with a point-like out-of-plane magnetic moment m (fig. S2). Figure 2C summarizes ~1700 such fits, accumulated over four different ranges of magnetic field. Throughout the measured range, the spatial distribution of reversal events is random (Fig. 2D, inset, and fig. S3), suggesting weak interactions between neighboring islands and supporting the conclusion that superparamagnetism in Cr-doped BiSbTe films is characterized by aggregations of dopant atoms. The deviation of the Hall resistance from its saturation value begins around $\mu_0 H = 0$ and is accompanied by the reversal of nanoscale moments with average $\overline{m} = 3 \times 10^4 \mu_B$ (Fig. 2, C and D). Given an average saturation magnetization of ~ $3\mu_B$/Cr atom as obtained from global magnetization measurements (fig. S4), the estimated average diameter of these flipping islands is d = 51 nm for our 7-nm-thick film, considerably below our spatial resolution of ~300 nm. However, as the field is increased toward H_c, a pronounced change in the

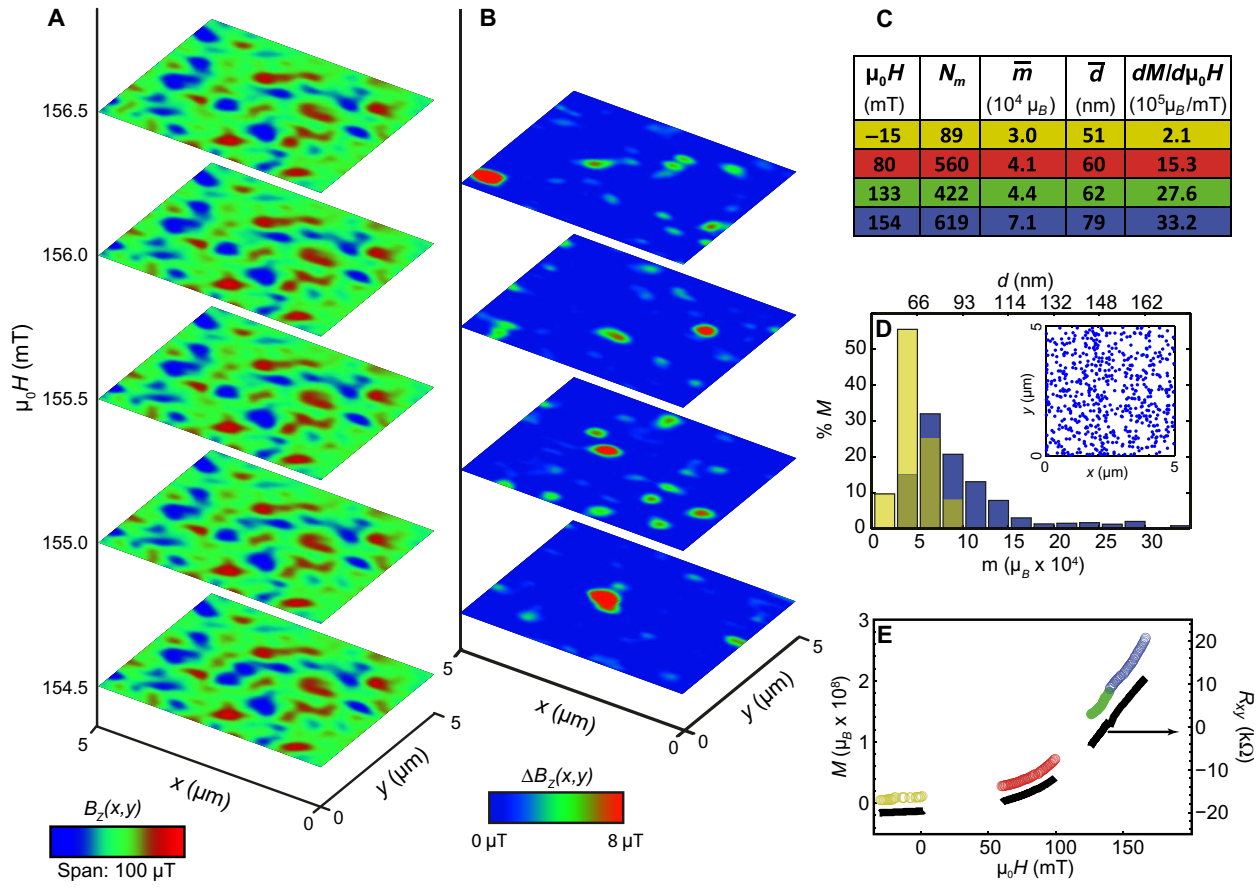

Fig. 2. Magnetization reversal dynamics. (**A**) Sequence of SOT magnetic images $B_z(x,y)$ taken at consecutive magnetic fields in 0.5 mT steps at T = 250 mK. (**B**) Differential images $\Delta B_z(x,y)$ obtained by subtracting pairs of consecutive $B_z(x,y)$ images in (A) showing the isolated magnetic reversal events (red) of the superparamagnetic moments (see movie S1). (**C**) Statistical analysis of 1690 reversal events attained over ranges of magnetic fields centered around four $\mu_0 H$ values: total number of moment reversals N_m, average magnetic moment $\overline{m}$, average superparamagnetic island diameter $\overline{d}$, and rate of the magnetization change $dM/d(\mu_0 H)$ over the given range. (**D**) Chart of relative contribution of different moment sizes m to the total magnetization change M within two field ranges centered at $\mu_0 H = -15$ mT (yellow) and $\mu_0 H = 154$ mT (blue). Inset: Location of the moment reversals within the field range around $\mu_0 H = 154$ mT. (**E**) Cumulative magnetization change M due to moment reversals m over four field ranges (left axis, colored symbols) and the simultaneously acquired R_{xy} (right axis, black). The total magnetization in each range is offset by an arbitrary constant.

moment distribution is observed with a shift to higher m values and appearance of a long tail of large moments with $m \geq 10^5 \mu_B$ (Fig. 2, C and D). The microscopic reversal moments m can be summed to obtain the net change in magnetization M over a continuous field range (Fig. 2E). Comparison with simultaneously acquired R_{xy} shows a qualitative match, implying that the behavior of the transport coefficients through the transition is mainly determined by the underlying change in magnetization. Superparamagnetic behavior and a similar relationship between measured magnetization and transport coefficients were found in a second sample as well as in an Mn-doped Bi_2Te_3 film (see movie S2 and figs. S6 to S9).

Hysteretic magnetic transitions are a signature of metastability and typically display temporal relaxation via thermal activation or quantum tunneling. We probe magnetic relaxation in real time by polarizing the system at $\mu_0 H = -1$ T and then ramping the field to a positive set point $\mu_0 H_{set}$. We then acquire repeated images of $B_z(x,y)$ while simultaneously monitoring electronic transport. No relaxation is observed on laboratory time scales for $\mu_0 H_{set} < 0$ in either magnetization or transport coefficients. Spontaneous relaxation begins to be evident at small positive fields ($\mu_0 H_{set}$ = 63 mT), manifesting as magnetic reversal events $\Delta B_z(x,y)$ and a slow upward drift of R_{xy}. The frequency and number of these reversals significantly increase near the coercive field at $\mu_0 H_{set}$ = 126 mT (Fig. 3, A and C).

The temporal relaxation measurements further corroborate the superparamagnetic behavior: at temperatures well below the blocking temperature, the magnetization of a superparamagnet is hysteretic, showing minimal relaxation at low fields. On approaching H_c, the magnetic anisotropy barrier U is reduced, leading to relaxation when $U \simeq k_B T$. Because U is proportional to the volume of the superparamagnetic particles, smaller islands undergo thermal activation at a lower field. Simultaneous transport measurements (Fig. 3D) indicate that the electronic transition closely tracks the magnetic relaxation, with transport coefficient relaxation evident at $\mu_0 H_{set}$ = 63 mT and pronounced at 126 mT, in accord with the total temporal change in magnetization extracted from the SOT data (Fig. 3C).

The plateau transition observed in electronic transport appears to be mainly dictated by the underlying magnetic reversal. Surprisingly, however, we find that the dynamics of the magnetic system can, in turn, be influenced by the electronic system. To explore this effect, we perform a

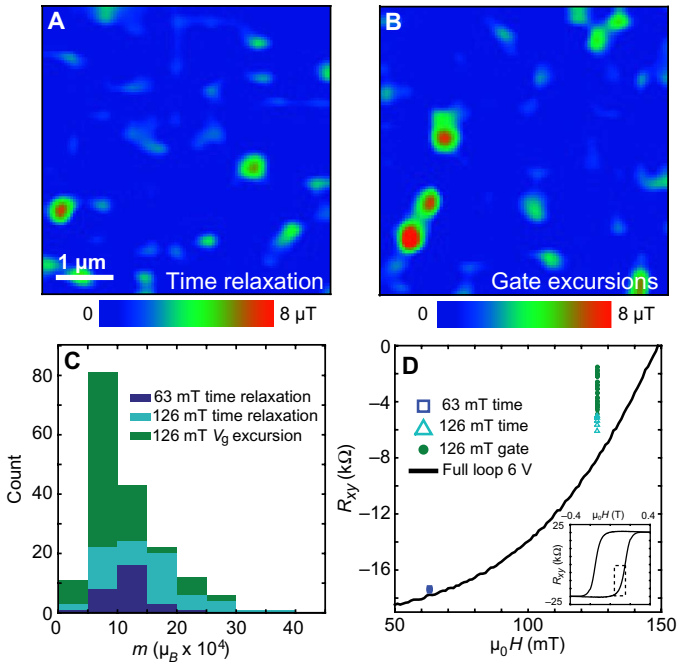

Fig. 3. Temporal and back gate–induced relaxation of the superparamagnetic state. (**A**) Differential image $\Delta B_z(x,y)$ obtained by subtraction of two consecutive images acquired at constant $\mu_0 H_{set}$ = 126 mT and V_g = 6 V after a field ramp from −1 T. Image acquisition time is 200 s with 50-s wait time between images. (**B**) Same as (A) with gate excursion progressively increasing from ΔV_g = 0.1 to 1.1 V in-between consecutive images. (**C**) Histogram of the temporal relaxation process showing the moment reversals m attained from four consecutive $\Delta B_z(x,y)$ images at $\mu_0 H_{set}$ = 63 mT (dark blue) and at $\mu_0 H_{set}$ = 126 mT (light blue), and of V_g-induced relaxation at $\mu_0 H_{set}$ = 126 mT acquired after the temporal relaxation of 20 min (green). (**D**) R_{xy} as a function of field (black) and during relaxation at a fixed field taken simultaneously with the magnetic imaging. Temporal relaxation over 20 min is more pronounced at 126 mT (light blue) than at 63 mT (dark blue). V_g excursions (green) induce large relaxation at 126 mT. Inset: Full R_{xy} hysteresis loop showing the region of interest.

sequence of magnetic imaging scans at 126 mT interspersing consecutive scans with small excursions of the back-gate voltage ΔV_g (Fig. 3B). All imaging scans are taken at a gate voltage of 6 V. Between scans, the gate is ramped at 500 mV/s to a voltage 6 V + ΔV_g and back to 6 V, with a wait time of a few seconds at the extremal value. Remarkably, even small $\Delta V_g \sim 1$ V excursions significantly enhance the relaxation of the superparamagnetic islands, as is evident from the statistics of the observed moment reversals (Fig. 3C). This enhancement, in turn, is evident in the transport coefficients, as shown in Fig. 3D.

A full comparison of the effects of applied magnetic field, gate voltage, and time on transport coefficients is presented in Fig. 4C, which shows a unified parametric plot of the transport coefficient vector (R_{xx}, R_{xy}). On this plot, the large magnetic hysteresis evident in Fig. 4 (A and B) is absent, demonstrating that the relation between R_{xx} and R_{xy} (at a given V_g) is a universal function determined by the magnetization. Within a single constant-V_g arc-shaped plot, zero net magnetization corresponds to the maximum of the arc at R_{xy} = 0, whereas the varying Hall angle along the arc reflects the varying sample magnetization. Variable V_g traces over ΔV_g = ±30 V at $\mu_0 H$ = ±1 T, marked in black, show contours of variable Fermi level at constant saturated magnetization. Note that at full saturation, variable V_g data retrace the same path upon repetition.

On this plot, the temporal relaxation of transport coefficients (fig. S13) is seen to track constant V_g arcs, implying that temporal magnetic relaxation is the dominant mechanism and consistent with the scanning magnetometry results (Fig. 4, C and D, gray dots along V_g = 6 V arc). Again, consistent with magnetometry data, V_g excursions markedly enhance the magnetization relaxation in the metastable regime (Fig. 4, C and D). The blue trace shows the evolution of the transport coefficients during six successive V_g excursions, with ΔV_g increasing from ±1 to ±3 V at a constant field of 126 mT. Successive V_g sweeps do not retrace each other, consistent with an irreversible change in the net magnetization. Repeating the same experiment for larger excursion of ΔV_g = ±30 V, the magnetization is observed to rapidly relax, nearly reaching complete saturation (cyan in Fig. 4, C and D). As Fig. 4C makes clear, the gate-induced magnetic relaxation is strongly dependent on maximum extent of the voltage excursion, although we find it to be independent of sweep direction and rate.

Strikingly, despite the marked effect of gate voltage variations on magnetic relaxation, field sweeps at different values of V_g show only small deviations in the coercive field (Fig. 4, A and B), indicating that carrier density has little effect on the average magnetization. These seemingly contradictory observations can be qualitatively understood by invoking the strongly disordered nature of the superparamagnetic state. In our strongly disordered system, the global gap in the density of states is bridged by a proliferation of subgap states induced by the random polarization of the superparamagnetic islands, possibly leading to electron-hole puddles (*27*) rather than a hard gap. These localized states can, in turn, mediate local FM interactions. V_g excursions modify the magnetic anisotropy energy of individual islands through the strong dependence of density of states on position and energy, randomly changing the magnetic potential landscape without significantly changing the average properties of the magnetic disorder potential (and thus the coercive field measured at fixed V_g). However, unlike in QH systems, the magnetic disorder is not quenched: the weakly interacting superparamagnetic islands are metastable and subject to irreversible relaxation. When the applied field is oriented opposite to the net magnetization, some local configurations are separated from the ground state by a small energy barrier U. Any local perturbation, including a modulation of local density of states, can cause an irreversible flip, leading to rapid stimulated relaxation upon repeated excursions of V_g. Our statistical analysis of temporal relaxation (fig. S15) shows that gate voltage does modulate the average size of the flipping moments for the same applied magnetic field. This again suggests that carriers mediate magnetic interactions.

DISCUSSION

In conclusion, we have imaged the magnetic structure of Cr-doped thin films of $(Bi,Sb)_2Te_3$ and found it to be strongly disordered. The magnetic reversal transition and its temporal relaxation are mediated by isolated nanoscale island reversals rather than domain wall motion, pointing to a superparamagnetic state composed of nearly noninteracting magnetic domains. Quantitative analysis shows that the observed dynamics account for most of the total magnetic moment, excluding the possibility of an underlying uniform FM state. Unexpectedly, gate voltage modulation strongly enhances the magnetic

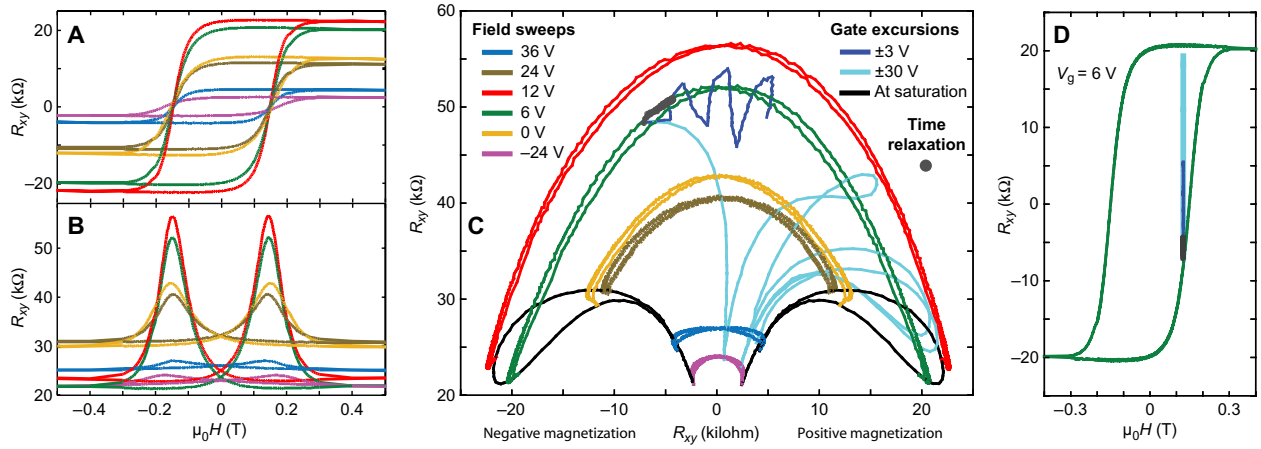

Fig. 4. Transport measurements and universal plot of magnetic relaxation. (**A** and **B**) R_{xy} (A) and R_{xx} (B) versus applied field at T = 250 mK and different V_g showing magnetic hysteresis with similar H_c. (**C**) Same data plotted as universal arc-like curves of R_{xx} versus R_{xy} at various V_g. Extrema of the arcs correspond to saturation magnetization at −1 T (+1 T) on the lower left (right) end of each arc. Gray dots indicate 60 min of temporal relaxation at $\mu_0 H_{set}$ = 126 mT and V_g = 6 V (see also fig. S13). Gate sweeps at $\mu_0 H = \pm 1$ T (black lines) trace the ends of the arcs and are reversible. Gate sweeps at 126 mT (blue and cyan) are metastable, inducing magnetic relaxation and propagation along the arcs from $R_{xy} < 0$ toward positive saturation. (**D**) R_{xy} relaxation data (gray, blue, and cyan) and R_{xy} field sweep at V_g = 6 V (green).

relaxation, suggesting that the charge carriers are involved in the mediation of magnetic interactions. Our results suggest that the quantum phase transition between QAH states can be strongly affected by the nature of the underlying magnetic transition, leading to deviations from the expected universal scaling of the plateau transition as indicated by recent transport studies (*31*). In particular, the magnetic disorder potential lowers the local QAH gap, lowering energy barriers for hopping conductivity across the sample bulk. Moreover, the large distribution in the flipping energy barrier U guarantees that, for zero magnetic field and finite temperature, some magnetic reversals will occur because of thermal fluctuations, further decreasing the average bulk gap. Although topological states are robust to disorder in the low temperature limit, as the temperature increases toward the blocking temperature T_B of the superparamagnetic islands, the enhanced dissipation due to thermally excited magnetization reversals is bound to destroy the protected state. Thus, nanoscale superparamagnetism may be one of the sources responsible for the fragility of the QAH state at elevated temperatures.

MATERIALS AND METHODS

Samples were grown by MBE on commercial $SrTiO_3$ substrates with dimensions of 5 × 5 × 0.5 mm^3. Substrates were typically annealed in oxygen at 925°C for 2.5 hours and were screened using atomic force microscopy (AFM) to make sure that the surface was atomically ordered with a root mean square roughness of less than 0.3 nm (fig. S16). Substrates were indium-mounted for growth in the MBE chamber and outgassed at a substrate temperature of 550°C for about 1 hour to remove any residual contamination before growth. The TI films were grown using elemental materials of at least 5N purity evaporated from Knudsen-type thermal cells at a growth rate of about 0.4 QL per minute at a temperature of 250°C, as measured by a pyrometer. The Cr, Bi, and Sb compositions were estimated from secondary ion mass spectrometry (SIMS) measurements on a similarly grown sample. The SIMS atomic percentages were calibrated using another sample of known composition that was measured at the same time.

SUPPLEMENTARY MATERIALS

Supplementary material for this article is available at http://advances.sciencemag.org/cgi/content/full/1/10/e1500740/DC1

Sample characterization

Fig. S1. STEM imaging and EDS elemental mapping of a Cr-doped $(Bi,Sb)_2Te_3$ film on $SrTiO_3$.

Magnetic moment fitting procedure

Fig. S2. Fitting procedure of magnetic moments.

Spatial distribution of the magnetization reversals

Fig. S3. Spatial distribution of the magnetization reversal process in 7-QL $Cr_{0.1}(Bi_{0.5}Sb_{0.5})_{1.9}Te_3$ sample at T = 250 mK.

Global magnetization studies

Fig. S4. SQUID magnetometry measurements of a ~40-QL-thick film.

Movies of the magnetic moment reversal dynamics

Fig. S5. Movie snapshot of magnetization reversal process in 7-QL $Cr_{0.1}(Bi_{0.5}Sb_{0.5})_{1.9}Te_3$ film at T = 250 mK.

Fig. S6. Movie snapshot of magnetization reversal process in 10-QL Cr-doped $(Bi,Sb)_2Te_3$ film at T = 250 mK.

Transport and superparamagnetic dynamics in 10-QL Cr-doped $(Bi,Sb)_2Te_3$ sample

Fig. S7. Magnetization reversal dynamics and transport coefficients in 10-QL-thick Cr-doped $(Bi,Sb)_2Te_3$ thin film at T = 250 mK.

Fig. S8. Scaling of the cumulative magnetization change and the transverse resistance in 10-QL Cr-doped $(Bi,Sb)_2Te_3$ film at T = 250 mK.

Transport and superparamagnetism in Mn-doped BiTe

Fig. S9. Transport and scanning magnetic imaging of 70-nm-thick Mn-doped BiTe sample at T = 250 mK.

Transport measurements

Fig. S10. Schematics of transport measurements.

Fig. S11. Temperature dependence of the transport coefficients in 7-QL $Cr_{0.1}(Bi_{0.5}Sb_{0.5})_{1.9}Te_3$ film.

Fig. S12. Gate voltage dependence of R_{xx} in 7-QL $Cr_{0.1}(Bi_{0.5}Sb_{0.5})_{1.9}Te_3$ sample.

Fig. S13. Temporal relaxation of transport coefficients near the coercive field in 7-QL $Cr_{0.1}(Bi_{0.5}Sb_{0.5})_{1.9}Te_3$ sample.

Fig. S14. Transport coefficients in 7-QL $Cr_{0.1}(Bi_{0.5}Sb_{0.5})_{1.9}Te_3$ sample with continuous gate excursions.

V_g dependence of the dynamics of magnetic relaxation

Fig. S15. Statistical analysis of temporal moment relaxation for different V_g values in 7-QL $Cr_{0.1}(Bi_{0.5}Sb_{0.5})_{1.9}Te_3$ film at T = 250 mK.

AFM of Cr-doped samples

Fig. S16. AFM topography images of the two studied Cr-doped $(Bi,Sb)_2Te_3$ samples.

REFERENCES AND NOTES

1. K. v. Klitzing, G. Dorda, M. Pepper, New method for high-accuracy determination of the fine-structure constant based on quantized Hall resistance. *Phys. Rev. Lett.* **45**, 494–497 (1980).
2. D. J. Thouless, M. Kohmoto, M. P. Nightingale, M. den Nijs, Quantized Hall conductance in a two-dimensional periodic potential. *Phys. Rev. Lett.* **49**, 405 (1982).
3. F. D. M. Haldane, Model for a quantum Hall effect without Landau levels: Condensed-matter realization of the "parity anomaly". *Phys. Rev. Lett.* **61**, 2015–2018 (1988).
4. C.-Z. Chang, J. Zhang, X. Feng, J. Shen, Z. Zhang, M. Guo, K. Li, Y. Ou, P. Wei, L.-L. Wang, Z.-Q. Ji, Y. Feng, S. Ji, X. Chen, J. Jia, X. Dai, Z. Fang, S.-C. Zhang, K. He, Y. Wang, L. Lu, X.-C. Ma, Q.-K. Xue, Experimental observation of the quantum anomalous Hall effect in a magnetic topological insulator. *Science* **340**, 167–170 (2013).
5. J. G. Checkelsky, R. Yoshimi, A. Tsukazaki, K. S. Takahashi, Y. Kozuka, J. Falson, M. Kawasaki, Y. Tokura, Trajectory of the anomalous Hall effect towards the quantized state in a ferromagnetic topological insulator. *Nat. Phys.* **10**, 731–736 (2014).
6. X. Kou, S.-T. Guo, Y. Fan, L. Pan, M. Lang, Y. Jiang, Q. Shao, T. Nie, K. Murata, J. Tang, Y. Wang, L. He, T.-K. Lee, W.-L. Lee, K. L. Wang, Scale-invariant quantum anomalous Hall effect in magnetic topological insulators beyond the two-dimensional limit. *Phys. Rev. Lett.* **113**, 137201 (2014).
7. A. J. Bestwick, E. J. Fox, X. Kou, L. Pan, K. L. Wang, D. Goldhaber-Gordon, Precise quantization of the anomalous Hall effect near zero magnetic field. *Phys. Rev. Lett.* **114**, 187201 (2015).
8. C.-Z. Chang, W. Zhao, D. Y. Kim, H. Zhang, B. A. Assaf, D. Heiman, S.-C. Zhang, C. Liu, M. H. W. Chan, J. S. Moodera, High-precision realization of robust quantum anomalous Hall state in a hard ferromagnetic topological insulator. *Nat. Mater.* **14**, 473–477 (2015).
9. A. Kandala, A. Richardella, S. Kempinger, C.-X. Liu, N. Samarth, Giant anisotropic magnetoresistance in a quantum anomalous Hall insulator. *Nat. Commun.* **6**, 7434 (2015).
10. M. Z. Hasan, C. L. Kane, *Colloquium*: Topological insulators. *Rev. Mod. Phys.* **82**, 3045–3067 (2010).
11. X.-L. Qi, S.-C. Zhang, Topological insulators and superconductors. *Rev. Mod. Phys.* **83**, 1057–1110 (2011).
12. M. Onoda, N. Nagaosa, Quantized anomalous Hall effect in two-dimensional ferromagnets: Quantum Hall effect in metals. *Phys. Rev. Lett.* **90**, 206601 (2003).
13. C. Liu, T. L. Hughes, X.-L. Qi, K. Wang, S.-C. Zhang, Quantum spin Hall effect in inverted type-II semiconductors. *Phys. Rev. Lett.* **100**, 236601 (2008).
14. Z. Qiao, S. A. Yang, W. Feng, W.-K. Tse, J. Ding, Y. Yao, J. Wang, Q. Niu, Quantum anomalous Hall effect in graphene from Rashba and exchange effects. *Phys. Rev. B* **82**, 161414(R) (2010).
15. R. Yu, W. Zhang, H.-J. Zhang, S.-C. Zhang, X. Dai, Z. Fang, Quantized anomalous Hall effect in magnetic topological insulators. *Science* **329**, 61–64 (2010).
16. M. Ezawa, Valley-polarized metals and quantum anomalous Hall effect in silicene. *Phys. Rev. Lett.* **109**, 055502 (2012).
17. K. F. Garrity, D. Vanderbilt, Chern insulators from heavy atoms on magnetic substrates. *Phys. Rev. Lett.* **110**, 116802 (2013).
18. G. Xu, J. Wang, C. Felser, X.-L. Qi, S.-C. Zhang, Quantum anomalous Hall effect in magnetic insulator heterostructure. *Nano Lett.* **15**, 2019–2023 (2015).
19. B. Huckestein, Scaling theory of the integer quantum Hall effect. *Rev. Mod. Phys.* **67**, 357–396 (1995).
20. J. Wang, B. Lian, S.-C. Zhang, Universal scaling of the quantum anomalous Hall plateau transition. *Phys. Rev. B* **89**, 085106 (2014).
21. A. Finkler, Y. Segev, Y. Myasoedov, M. L. Rappaport, L. Ne'eman, D. Vasyukov, E. Zeldov, M. E. Huber, J. Martin, A. Yacoby, Self-aligned nanoscale SQUID on a tip. *Nano Lett.* **10**, 1046–1049 (2010).
22. D. Vasyukov, Y. Anahory, L. Embon, D. Halbertal, J. Cuppens, L. Neeman, A. Finkler, Y. Segev, Y. Myasoedov, M. L. Rappaport, M. E. Huber, E. Zeldov, A scanning superconducting quantum interference device with single electron spin sensitivity. *Nat. Nanotechnol.* **8**, 639–644 (2013).
23. C.-Z. Chang, J. Zhang, M. Liu, Z. Zhang, X. Feng, K. Li, L.-L. Wang, X. Chen, X. Dai, Z. Fang, X.-L. Qi, S.-C. Zhang, Y. Wang, K. He, X.-C. Ma, Q.-K. Xue, Thin films of magnetically doped topological insulator with carrier-independent long-range ferromagnetic order. *Adv. Mater.* **25**, 1065–1070 (2013).
24. S. Kuroda, N. Nishizawa, K. Takita, M. Mitome, Y. Bando, K. Osuch, T. Dietl, Origin and control of high-temperature ferromagnetism in semiconductors. *Nat. Mater.* **6**, 440–446 (2007).
25. C.-Z. Chang, P. Tang, Y.-L. Wang, X. Feng, K. Li, Z. Zhang, Y. Wang, L. L. Wang, X. Chen, C. Liu, W. Duan, K. He, X.-C. Ma, Q.-K. Xue, Chemical-potential-dependent gap opening at the Dirac surface states of Bi_2Se_3 induced by aggregated substitutional Cr atoms. *Phys. Rev. Lett.* **112**, 056801 (2014).
26. I. Lee, C. K. Kim, J. Lee, S. J. L. Billinge, R. Zhong, J. A. Schneeloch, T. Liu, T. Valla, J. M. Tranquada, G. Gu, J. C. S. Davis, Imaging Dirac-mass disorder from magnetic dopant atoms in the ferromagnetic topological insulator $Cr_x(Bi_{0.1}Sb_{0.9})_{2-x}Te_3$. *Proc. Natl. Acad. Sci. U.S.A.* **112**, 1316–1321 (2015).
27. H. Beidenkopf, P. Roushan, J. Seo, L. Gorman, I. Drozdov, Y. S. Hor, R. J. Cava, A. Yazdani, Spatial fluctuations of helical Dirac fermions on the surface of topological insulators. *Nat. Phys.* **7**, 939–943 (2011).
28. M. Yamanouchi, J. Ieda, F. Matsukura, S. E. Barnes, S. Maekawa, H. Ohno, Universality classes for domain wall motion in the ferromagnetic semiconductor (Ga,Mn)As. *Science* **317**, 1726–1729 (2007).
29. A. L. Balk, M. E. Nowakowski, M. J. Wilson, D. W. Rench, P. Schiffer, D. D. Awschalom, N. Samarth, Measurements of nanoscale domain wall flexing in a ferromagnetic thin film. *Phys. Rev. Lett.* **107**, 077205 (2011).
30. X. Kou, L. He, M. Lang, Y. Fan, K. Wong, Y. Jiang, T. Nie, W. Jiang, P. Upadhyaya, Z. Xing, Y. Wang, F. Xiu, R. N. Schwartz, K. L. Wang, Manipulating surface-related ferromagnetism in modulation-doped topological insulators. *Nano Lett.* **13**, 4587–4593 (2013).
31. X. Kou, L. Pan, J. Wang, Y. Fan, E. S. Choi, W.-L. Lee, T. Nie, K. Murata, Q. Shao, S.-C. Zhang, K. L. Wang, Metal-to-insulator switching in quantum anomalous Hall states. *Nat. Commun.* **6**, 8474 (2015).

Acknowledgments: We thank E. Berg for illuminating discussions. **Funding:** This work was supported by the Minerva Foundation with funding from the German Federal Ministry of Education and Research and by the Israel Science Foundation (grant no. 132/14). N.S., A.R., A.K., and S.K. acknowledge support from DARPA (Defense Advanced Research Projects Agency) MESO (Mesodynamic Architectures) (grant no. N66001-11-1-4110), ONR (Office of Naval Research) (grant no. N00014-12-1-0117), and ARO MURI (Army Research Office Multidisciplinary University Research Initiative) (grant no. W911NF-12-1-0461), as well as use of the NSF National Nanofabrication Users Network Facility at the Pennsylvania State University. A.F.Y. acknowledges the support of Goldschleger Center for Nanophysics. **Author contributions:** E.O.L., A.F.Y., and J.C. performed the magnetic imaging and transport measurements. A.R., A.K., and N.S. fabricated and characterized the samples. H.R.N. fabricated the SOTs. Y.A. and A.Y.M. developed the numerical data analysis. S.K. performed global magnetization studies. M.E.H. developed the SOT readout system. Y.M. prepared the samples. E.O.L., A.F.Y., E.Z., A.R., and N.S. wrote the paper with contributions from other authors. **Competing interests:** The authors declare that they have no competing interests. **Data and materials availability:** All data needed to evaluate the conclusions in the paper are present in the paper and/or the Supplementary Materials. Additional data related to this paper may be requested from the authors.

Submitted 8 June 2015
Accepted 26 August 2015
Published 6 November 2015
10.1126/sciadv.1500740

Citation: E. O. Lachman, A. F. Young, A. Richardella, J. Cuppens, H. R. Naren, Y. Anahory, A. Y. Meltzer, A. Kandala, S. Kempinger, Y. Myasoedov, M. E. Huber, N. Samarth, E. Zeldov, Visualization of superparamagnetic dynamics in magnetic topological insulators. *Sci. Adv.* **1**, e1500740 (2015).